Application and Evaluation of the Common Circles Method

Michael Quellmalz* Mia Kvåle Løvmo† Simon Moser† Franziska Strasser†
Monika Ritsch-Marte†

Abstract

We investigate the application of the common circle method for estimating sample motion in optical diffraction tomography (ODT) of sub-millimeter sized biological tissue. When samples are confined via contact-free acoustical force fields, their motion must be estimated from the captured images. The common circle method identifies intersections of Ewald spheres in Fourier space to determine rotational motion. This paper presents a practical implementation, incorporating temporal consistency constraints to achieve stable reconstructions. Our results on both simulated and real-world data demonstrate that the common circle method provides a computationally efficient alternative to full optimization methods for motion detection.

Keywords. Diffraction tomography, motion detection, Fourier diffraction theorem, common circle method, acoustic trapping, optical imaging.

Math Subject Classifications. 92C55, 78A46, 94A08, 42B05.

1 Introduction

We consider the tomographic imaging of sub-millimeter sized biological samples by means of *optical diffraction tomography (ODT)* [7, 15, 37]. In ODT, the object is illuminated from different angles to reconstruct its 3D refractive index. While traditional sample immobilization, e.g. in gel, may restrict biological processes, contact-free methods utilizing optical [14] or acoustical tweezers [8, 38] allow imaging of cells in their natural environment. However, the motion parameters are not known exactly and must be estimated from the captured images.

In standard computed tomography, optical diffraction is negligible because the wavelength of x-rays is much smaller than object features, allowing for a straight-line light propagation model. In contrast, our ODT setup involves µm-sized biological cells imaged with visible light, where diffraction effects require more sophisticated wave propagation models.

Therefore, the *common line method* [9, 31, 36, 39, 41] for orientation detection in x-ray tomography, which uses that each x-ray image becomes a plane in Fourier space, is not applicable. Under the Born approximation, each ODT measurement corresponds to an Ewald sphere in Fourier space, cf. [28]. The *common circle method* [34], see also [4], reconstructs the motion of the imaged object by identifying the intersections (common circles) of these sphere, see Figure 1 left.

While the theoretical foundations of the common circle method were established in [34], this paper focuses on the application to real-world data. We obtain stable reconstructions by adding additional regularization and ensuring temporal consistency. Finally, we provide a quantitative comparison with the full optimization approach [27] for ODT motion detection,

*TU Berlin, quellmalz@math.tu-berlin.de
†Medical University of Innsbruck, Loevmo.Mia@i-med.ac.at, Simon.Moser@i-med.ac.at, Monika.Ritsch-Marte@i-med.ac.at

which simultaneously reconstructs object and motion based on the beam propagation method, see also [23]. In comparison, the common circle method is less accurate, but it is considerably faster and does not require an initialization of the rotation parameters, therefore providing a good initial guess for more computationally intensive techniques.

This paper is structured as follows. Section 2 outlines the theoretical basis of ODT and the common circle method. Section 3 describes the reconstruction approach. Section 4 presents our numerical data processing and reconstruction. Conclusions are drawn in Section 5.

2 Diffraction Tomography

In this section, we describe the setup of diffraction tomography with a moving object and the common circle method for reconstructing the rotations, whose theoretical foundations were derived in [34].

2.1 Fourier Diffraction Theorem

We start with the model of *optical diffraction tomography* for a fixed object, see more detail in [18, 19, 42]. The unknown object is illuminated by a *plane wave*

$$u^{\mathrm{inc}}(\boldsymbol{x}) \coloneqq \mathrm{e}^{\mathrm{i}k_0 x_3}, \quad \boldsymbol{x} \in \mathbb{R}^3, \tag{2.1}$$

which propagates in direction $\boldsymbol{e}^3 = (0,0,1)^\top$ with wave number $k_0 = 2\pi n_0/\lambda_0$, where n_0 is the constant refractive index of the surrounding medium and λ_0 is the wavelength of the incident field. Let $n(\boldsymbol{x})$ denote the *refractive index* at position $\boldsymbol{x} \in \mathbb{R}^3$. We have $n(\boldsymbol{x}) = n_0$ outside the object. The *scattering potential* or object function

$$f(\boldsymbol{x}) \coloneqq k_0^2 \left(\frac{n(\boldsymbol{x})^2}{n_0^2} - 1 \right) \tag{2.2}$$

vanishes outside the object. We assume f is piecewise continuous and compactly supported. The incident wave u^{inc} induces a *scattered wave* u^{sca} that solves the partial differential equation

$$-(\Delta + k_0^2) u^{\mathrm{sca}}(\boldsymbol{x}) = f(\boldsymbol{x}) \left(u^{\mathrm{sca}}(\boldsymbol{x}) + u^{\mathrm{inc}}(\boldsymbol{x}) \right), \qquad \boldsymbol{x} \in \mathbb{R}^3. \tag{2.3}$$

More specifically, u^{sca} is the outgoing solution, which fulfills the Sommerfeld radiation condition

$$\lim_{r\to\infty} \max_{\|\boldsymbol{x}\|=r} \|\boldsymbol{x}\| \left| \langle \nabla u^{\mathrm{sca}}(\boldsymbol{x}), \tfrac{\boldsymbol{x}}{\|\boldsymbol{x}\|} \rangle - \mathrm{i}k_0 u^{\mathrm{sca}}(\boldsymbol{x}) \right| = 0.$$

If f is sufficiently small, we neglect $f u^{\mathrm{sca}}$ on the right-hand side of (2.3) to obtain the *Born approximation* u of the scattered field u^{sca}, determined by the Helmholtz equation

$$-(\Delta + k_0^2) u(\boldsymbol{x}) = f(\boldsymbol{x}) u^{\mathrm{inc}}(\boldsymbol{x}). \tag{2.4}$$

In the following, we assume the Born approximation to be valid, which holds for small objects which mildly scatter, in particular that total phase shift through the object being much less than 2π, cf. [11, 15, 43].

We denote the measurements of the scattered wave at the plane $\{\boldsymbol{x} \in \mathbb{R}^3 : x_3 = r_{\mathrm{M}}\}$ at r_{M} outside the object by

$$m(x_1, x_2) \coloneqq u(x_1, x_2, r_{\mathrm{M}}), \qquad (x_1, x_2) \in \mathbb{R}^d.$$

We define the d-dimensional *Fourier transform* of an integrable function $g\colon \mathbb{R}^d \to \mathbb{C}$ by

$$\mathcal{F}_d[g](\hat{\boldsymbol{x}}) \coloneqq (2\pi)^{-d/2} \int_{\mathbb{R}^d} g(\boldsymbol{x})\, \mathrm{e}^{-\mathrm{i}\langle \boldsymbol{x}, \hat{\boldsymbol{x}} \rangle}\, \mathrm{d}\boldsymbol{x}, \quad \hat{\boldsymbol{x}} \in \mathbb{R}^d,$$

and the ball of radius $r > 0$ by

$$\mathcal{B}_r^d := \{\boldsymbol{x} \in \mathbb{R}^d : \|\boldsymbol{x}\| < r\}, \qquad d \in \mathbb{N},\ r > 0.$$

The *Fourier diffraction theorem* relates the 2D Fourier transform of the measurements m to the 3D Fourier transform of the scattering potential f, see [15, 18, 29, 42]. We have

$$\mathcal{F}_2[m](\boldsymbol{k}) = \sqrt{\frac{\pi}{2}}\,\frac{\mathrm{i}\mathrm{e}^{\mathrm{i}\kappa(\boldsymbol{k})r_{\mathrm{M}}}}{\kappa(\boldsymbol{k})}\mathcal{F}_3[f]\left(\boldsymbol{h}(\boldsymbol{k})\right) \qquad \forall\, \boldsymbol{k} = (k_1, k_2) \in \mathcal{B}_{k_0}^2, \tag{2.5}$$

where $\boldsymbol{h}\colon \mathcal{B}_{k_0}^2 \to \mathbb{R}^3$ is defined by

$$\boldsymbol{h}(\boldsymbol{k}) := \begin{pmatrix} \boldsymbol{k} \\ \kappa(\boldsymbol{k}) - k_0 \end{pmatrix}, \quad \text{and} \quad \kappa(\boldsymbol{k}) := \sqrt{k_0^2 - \|\boldsymbol{k}\|^2}.$$

The left-hand side of (2.5) is the Fourier transform of the measured 2D image m, and the right-hand side is the 3D Fourier transform of f evaluated on a hemisphere whose north pole is the origin $\mathbf{0}$, see Figure 1.

2.2 Motion of the object

The object is exposed to a rigid motion depending on time $t \in [0, T]$, such that the scattering potential of the moving object is

$$f_t(\boldsymbol{x}) = f(R_t(\boldsymbol{x} - \boldsymbol{d}_t)), \qquad \boldsymbol{x} \in \mathbb{R}^3, \tag{2.6}$$

with a rotation matrix

$$R_t \in \mathrm{SO}(3) := \{Q \in \mathbb{R}^{3\times 3} : Q^\top Q = I,\ \det Q = 1\},$$

and a translation vector $\boldsymbol{d}_t \in \mathbb{R}^3$. The incident wave (2.1) and the measurement plane $\{\boldsymbol{x} \in \mathbb{R}^3 : x_3 = r_{\mathrm{M}}\}$ stay the same as above. The scattered wave u_t is the solution of (2.4) with f replaced by f_t. Denoting the measurements by

$$m\colon [0, T] \times \mathbb{R}^2 \to \mathbb{R}, \qquad m_t(x_1, x_2) := u_t(x_1, x_2, r_{\mathrm{M}}),$$

the Fourier diffraction theorem (2.5) becomes [34]

$$\mathcal{F}_2[m_t](\boldsymbol{k}) = \sqrt{\frac{\pi}{2}}\,\frac{\mathrm{i}\mathrm{e}^{\mathrm{i}\kappa(\boldsymbol{k})r_{\mathrm{M}}}}{\kappa(\boldsymbol{k})}\mathcal{F}_3[f]\left(R_t\boldsymbol{h}(\boldsymbol{k})\right)\mathrm{e}^{-\mathrm{i}\langle \boldsymbol{d}_t, \boldsymbol{h}(\boldsymbol{k})\rangle}, \qquad \boldsymbol{k} \in \mathcal{B}_{k_0}^2.$$

2.3 Common Circle Method

The *scaled squared energy*

$$\nu_t\colon \mathcal{B}_{k_0}^2 \to [0, \infty), \qquad \nu_t(\boldsymbol{k}) := \frac{2}{\pi}\kappa^2(\boldsymbol{k})\left|\mathcal{F}_2[m_t](\boldsymbol{k})\right|^2 \tag{2.7}$$

depends only on the measurements m_t, $t \in [0, T]$, and is related to the scattering potential f via

$$\nu_t(\boldsymbol{k}) = \left|\mathcal{F}_3[f](R_t\boldsymbol{h}(\boldsymbol{k}))\right|^2, \qquad \boldsymbol{k} \in \mathcal{B}_{k_0}^2.$$

For every t, we see that ν_t provides the Fourier transform of f on the set

$$\mathcal{H}_t := \left\{R_t\boldsymbol{h}(\boldsymbol{k}) : \boldsymbol{k} \in \mathcal{B}_{k_0}^2\right\} = \{R_t\hat{\boldsymbol{x}} : \|\hat{\boldsymbol{x}} + k_0\boldsymbol{e}^3\| = k_0,\ y_3 > -k_0\}, \quad t \in [0, T],$$

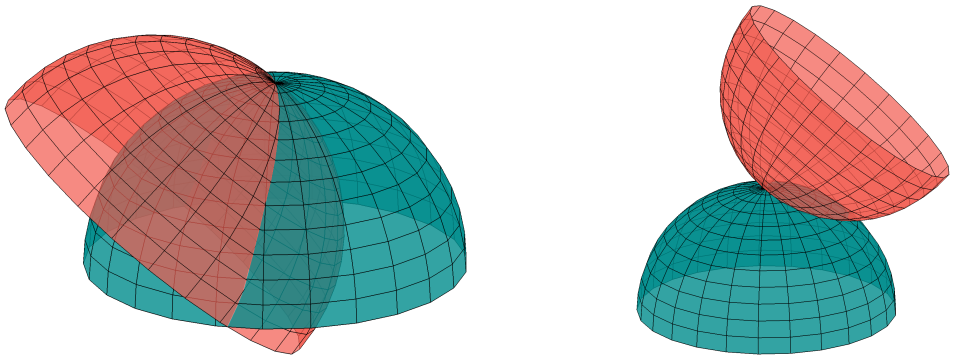

Figure 1: Illustration of the common circles as intersections of the Ewald spheres. Left: Two hemispheres $\mathcal{H}_0$ (green) and $\mathcal{H}_t$ (red) intersect in a common circle. The north pole of both hemispheres is at $\mathbf{0}$. Right: For real-valued (lossless) interactions, a dual common circle at the intersection of $\mathcal{H}_0$ (green) and $-\mathcal{H}_t$ (red) exists. Data must agree on the two intersections.

which is a hemisphere with radius k_0 and center $-k_0 R_t \boldsymbol{e}^3$. For two time steps s, t, the intersection $\mathcal{H}_s \cap \mathcal{H}_t$, $s \neq t$ is an arc of a circle, see Figure 1 left. The idea is to parameterize the common circle by pairs $\boldsymbol{k}_{s,t}$, $\boldsymbol{k}_{t,s}$ such that $R_s \boldsymbol{h}(\boldsymbol{k}_{s,t}) = R_t \boldsymbol{h}(\boldsymbol{k}_{t,s}) \in \mathcal{H}_s \cap \mathcal{H}_t$, then we have

$$\nu_s(\boldsymbol{k}_{s,t}) = \nu_t(\boldsymbol{k}_{t,s}).$$

If f is real-valued, there is no absorption, and its Fourier transform is conjugate symmetric, i.e., $\mathcal{F}_3[f](\hat{\boldsymbol{x}}) = \overline{\mathcal{F}_3[f](-\hat{\boldsymbol{x}})}$ for all $\hat{\boldsymbol{x}} \in \mathbb{R}^3$. Then there is another pair of *dual common circles* in the intersection $\mathcal{H}_s \cap (-\mathcal{H}_t)$, where the measurements must agree, see Figure 1 right.

The next theorem states that the incremental rotation $R_s^\top R_t$ can be determined from finding the common circle pairs in the data ν_s, ν_t. We represent a rotation $Q \in \mathrm{SO}(3)$ via Euler angles,

$$Q = Q^{(3)}(\varphi)\, Q^{(2)}(\theta)\, Q^{(3)}(\psi), \quad \varphi, \psi \in [0, 2\pi),\ \theta \in [0, \pi], \tag{2.8}$$

where

$$Q^{(2)}(\alpha) := \begin{pmatrix} \cos\alpha & 0 & \sin\alpha \\ 0 & 1 & 0 \\ -\sin\alpha & 0 & \cos\alpha \end{pmatrix} \quad \text{and} \quad Q^{(3)}(\alpha) := \begin{pmatrix} \cos\alpha & -\sin\alpha & 0 \\ \sin\alpha & \cos\alpha & 0 \\ 0 & 0 & 1 \end{pmatrix}$$

are rotations around the y and z axis, respectively.

Theorem 2.1 ([34, Thm 3.6])**.** *Let $s, t \in [0, T]$. Assume that there exist unique angles $\varphi, \psi \in [0, 2\pi)$ and $\theta \in [0, \pi]$ such that*

$$\nu_s(\boldsymbol{\gamma}^{\varphi,\theta}(\beta)) = \nu_t(\boldsymbol{\gamma}^{\pi-\psi,\theta}(-\beta)) \quad \forall\, \beta \in [-\tfrac{\pi}{2}, \tfrac{\pi}{2}] \quad \textit{and} \tag{2.9}$$

$$\nu_s(\boldsymbol{\gamma}^{*,\varphi,\theta}(\beta)) = \nu_t(\boldsymbol{\gamma}^{*,\pi-\psi,\theta}(\beta)) \quad \forall\, \beta \in [-\tfrac{\pi}{2}, \tfrac{\pi}{2}], \tag{2.10}$$

where

$$\boldsymbol{\gamma}^{\varphi,\theta}(\beta) := \frac{k_0}{2} \sin\theta \cdot (\cos\beta - 1) \begin{pmatrix} \cos\varphi \\ \sin\varphi \end{pmatrix} + k_0 \cos\tfrac{\theta}{2}\, \sin\beta \begin{pmatrix} -\sin\varphi \\ \cos\varphi \end{pmatrix} \quad \textit{and} \tag{2.11}$$

$$\boldsymbol{\gamma}^{*,\varphi,\theta}(\beta) := -\frac{k_0}{2} \sin\theta \cdot (\cos\beta - 1) \begin{pmatrix} \cos\varphi \\ \sin\varphi \end{pmatrix} - k_0 \sin\tfrac{\theta}{2}\, \sin\beta \begin{pmatrix} -\sin\varphi \\ \cos\varphi \end{pmatrix}. \tag{2.12}$$

Then the incremental rotation is

$$R_s^\top R_t = Q^{(3)}(\varphi) Q^{(2)}(\theta) Q^{(3)}(\psi).$$

The elliptic arcs (2.11) and (2.12) provide parameterizations of the common circle $\mathcal{H}_s \cap \mathcal{H}_t$ and the dual common circle $\mathcal{H}_s \cap (-\mathcal{H}_t)$, respectively. In general, it is not known when the uniqueness assumption in the last theorem is fulfilled. However, it was shown that under certain assumptions on f and if the measurements cover the whole SO(3), the object is uniquely determined [20].

2.4 Infinitesimal Common Circle Method

The infinitesimal common circle method relies on comparing derivatives of ν_t. We assume that the rotation R_t is continuously differentiable in time $t \in [0, T]$. The *angular velocity* corresponding to R_t is the unique vector $\boldsymbol{\omega}_t \in \mathbb{R}^3$ satisfying

$$R_t^\top R_t' \boldsymbol{y} = \boldsymbol{\omega}_t \times \boldsymbol{y} \qquad \forall\, t \in [0, T],\ \boldsymbol{y} \in \mathbb{R}^3.$$

We express $\boldsymbol{\omega}_t$ in cylindrical coordinates

$$\boldsymbol{\omega}_t = (\rho_t \cos\phi_t,\ \rho_t \sin\phi_t,\ \zeta_t)^\top, \qquad \phi_t \in [0, \pi), \quad \rho_t,\ \zeta_t \in \mathbb{R}. \tag{2.13}$$

Theorem 2.2 ([34, Thm 4.2])**.** *Let the rotation matrix $R \in C^1([0, T] \to \mathrm{SO}(3))$ be continuously differentiable and $t \in [0, T]$. Let further $\phi \in [0, \pi)$ be a unique angle with the property that there exist $\rho, \zeta \in \mathbb{R}$ such that*

$$\partial_t \nu_t \left(r \begin{pmatrix} \cos\phi \\ \sin\phi \end{pmatrix} \right) = \left(\rho \left(k_0 - \sqrt{k_0^2 - r^2} \right) + r\zeta \right) \left\langle \nabla \nu_t \left(r \begin{pmatrix} \cos\phi \\ \sin\phi \end{pmatrix} \right), \begin{pmatrix} -\sin\phi \\ \cos\phi \end{pmatrix} \right\rangle \quad \forall\, r \in (-k_0, k_0). \tag{2.14}$$

If there exist at least two values $r \in (-k_0, k_0) \setminus \{0\}$ such that $\left\langle \nabla \nu_t \left(r \begin{pmatrix} \cos\phi \\ \sin\phi \end{pmatrix} \right), \begin{pmatrix} -\sin\phi \\ \cos\phi \end{pmatrix} \right\rangle \neq 0$, then the angular velocity (2.13) is given by $\boldsymbol{\omega}_t = (\rho \cos\phi, \rho \sin\phi, \zeta)^\top$.

Recently, it was shown [10] that (2.14) always has a unique solution if the object f obeys a certain asymmetry condition.

Given the reconstructed angular velocity $\boldsymbol{\omega}_t$ for all t and an initial rotation $R_0 \in \mathrm{SO}(3)$, the rotation R_t is the unique solution of the linear initial value problem

$$R_t' = R_t W_t, \quad t \in [0, T], \tag{2.15}$$

see [34, Thm 4.3], with the skew-symmetric matrix

$$W_t = \begin{pmatrix} 0 & -\omega_{t,3} & \omega_{t,2} \\ \omega_{t,3} & 0 & -\omega_{t,1} \\ -\omega_{t,2} & \omega_{t,1} & 0 \end{pmatrix}, \qquad \boldsymbol{\omega}_t = (\omega_{t,1}, \omega_{t,2}, \omega_{t,3})^\top.$$

3 Reconstruction of the Rotation

In this section, we describe numerical algorithms to reconstruct the rotations, assuming that ν_t from (2.7) are given. We start with the infinitesimal common circle method, serving as initial guess for the direct method.

3.1 Infinitesimal Common Circle Method

3.1.1 Estimate of the Angular Velocity

Let $t \in (0, T)$. We reconstruct the angular velocity $\boldsymbol{\omega}_t = (\rho_t \cos\phi_t, \rho_t \sin\phi_t, \zeta_t)$ using a variational approach for Theorem 2.2. Following [34], we set for $r \in (-k_0, k_0)$ and $\phi \in [0, \pi)$,

$$\begin{aligned} g_\phi(r) &:= \partial_t \nu_t(r\cos(\phi), r\sin(\phi)), \\ p_\phi(r) &:= \frac{1}{r}(k_0 - \sqrt{k_0^2 - r^2})\, \partial_\phi \nu_t(r\cos(\phi), r\sin(\phi)), \\ q_\phi(r) &:= \partial_\phi \nu_t(r\cos(\phi), r\sin(\phi)), \end{aligned} \tag{3.1}$$

which depend only on the data ν_t. Then (2.14) becomes

$$g_{\phi_t}(r) = \rho_t\, p_{\phi_t}(r) + \zeta_t\, q_{\phi_t}(r), \qquad r \in (-k_0, k_0). \tag{3.2}$$

We use a least squares approach to solve (3.2) for ρ_t, ϕ_t and ζ_t. We minimize the functional

$$\mathcal{J}_t(\rho, \phi, \zeta) \coloneqq \|g_\phi - \rho\, p_\phi - \zeta\, q_\phi\|^2_{L^2(-k_0,k_0)}, \qquad \rho, \zeta \in \mathbb{R},\ \phi \in [0, \pi), \tag{3.3}$$

as follows. For every $\phi \in [0, \pi)$ on a fixed grid, we compute the minimizer of $\mathcal{J}(\cdot, \phi, \cdot)\colon \mathbb{R}^2 \to \mathbb{R}$ given by

$$\begin{pmatrix} \hat\rho(\phi) \\ \hat\zeta(\phi) \end{pmatrix} = \begin{pmatrix} \langle p_\phi, p_\phi\rangle & \langle p_\phi, q_\phi\rangle \\ \langle p_\phi, q_\phi\rangle & \langle q_\phi, q_\phi\rangle \end{pmatrix}^{-1} \begin{pmatrix} \langle g_\phi, p_\phi\rangle \\ \langle g_\phi, q_\phi\rangle \end{pmatrix}, \tag{3.4}$$

where $\langle \cdot, \cdot \rangle$ is the inner product on $L^2(-k_0, k_0)$ and we assume that p_ϕ and q_ϕ are linearly independent. For all such $\phi \in [0, \pi)$, we set $j_t(\phi) = \mathcal{J}_t(\hat\rho(\phi), \phi, \hat\zeta(\phi))$, and then $\hat\phi = \arg\min_{\phi\in[0,\pi)} j_t(\phi)$. Finally, we approximate the angular velocity $\boldsymbol{\omega}_t \approx (\hat\rho(\hat\phi)\cos\hat\phi,\ \hat\rho(\hat\phi)\sin\hat\phi,\ \hat\zeta(\hat\phi))$. The method is summarized in Algorithm 1, see [34, Algo 2].

Algorithm 1: Reconstruction of the angular velocity $\boldsymbol{\omega}_t$ with the infinitesimal method

Input: Scaled squared energy $\nu_t(r_n \cos\phi_\ell, r_n \sin\phi_\ell)$ from (2.7) on polar grid $r_n \in [0, k_0)$, $n = 1, \dots, N$, and $\phi_\ell \in [0, \pi)$, $\ell = 1, \dots, L$.

for $\ell = 1, \dots, L$ **do**

- Compute $g_{\phi_\ell}(r_n)$, $p_{\phi_\ell}(r_n)$, and $q_{\phi_\ell}(r_n)$, $n = 1, \dots, N$ by (3.1);
- Compute $\hat\rho(\phi_\ell)$ and $\hat\zeta(\phi_\ell)$ by (3.4);
- Compute $j(\phi_\ell) \coloneqq \sum_{n=1}^N |g_{\phi_\ell}(r_n) - \hat\rho(\hat\phi_\ell)\, p_{\phi_\ell}(r_n) - \hat\zeta(\hat\phi_\ell)\, q_{\phi_\ell}(r_n)|^2$

end

Set $\hat\phi$ as minimizer of $j(\phi_\ell)$ over $\ell = 1, \dots, L$;

Output: Angular velocity $\boldsymbol{\omega}_t \approx (\hat\rho(\hat\phi)\cos\hat\phi,\ \hat\rho(\hat\phi)\sin\hat\phi,\ \hat\zeta(\hat\phi))$.

The directional derivative $\partial_\phi \nu_t(r\cos\phi, r\sin\phi)$ in (3.1) can be computed from the measurements m_t via the following lemma.

Lemma 3.1. *Let $r \in (-k_0, k_0)$ and $\phi \in [0, \pi)$. Setting $M_t(\boldsymbol{x}) \coloneqq -\mathrm{i}\boldsymbol{x} m_t(\boldsymbol{x})$, we have*

$$\partial_\phi \nu_t(r\cos\phi, r\sin\phi) = \frac{4}{\pi}(k_0^2 - r^2)\ \mathrm{Re}\left(\mathcal{F}_2[m_t](r\cos\phi, r\sin\phi)\ \partial_\phi \mathcal{F}_2[M_t](r\cos\phi, r\sin\phi)\right).$$

Proof. Let $\boldsymbol{k} \in \mathcal{B}^2_{k_0}$. We note that $\partial_\phi \nu_t(r\cos\phi, r\sin\phi) = \left\langle \nabla \nu_t(r\cos\phi, r\sin\phi), \left(\begin{smallmatrix} -\sin\phi \\ \cos\phi \end{smallmatrix}\right)\right\rangle$. We have $\nabla \kappa^2(\boldsymbol{k}) = -2\boldsymbol{k}$. By (2.7), we see that

$$\nabla \nu_t(\boldsymbol{k}) = \tfrac{2}{\pi}\left(-2\boldsymbol{k}\,|\mathcal{F}_2[m_t](\boldsymbol{k})|^2 + \kappa^2(\boldsymbol{k}) 2\,\mathrm{Re}\left(\mathcal{F}_2[m_t](\boldsymbol{k}) \nabla \mathcal{F}_2[m_t](\boldsymbol{k})\right)\right).$$

The differentiation property of the Fourier transform yields $\nabla \mathcal{F}_2[m_t](\boldsymbol{k}) = \mathcal{F}_2[M_t](\boldsymbol{k})$. Inserting $\boldsymbol{k} = (r\cos\phi, r\sin\phi)^\top$ and using that $\langle \boldsymbol{k}, (-\sin\phi, \cos\phi)^\top\rangle = 0$ and $\kappa^2(r\cos\phi, r\sin\phi) = (k_0^2 - r^2)$, we obtain the assertion. □

3.1.2 Temporal Regularization of the Angular Velocity

In our application, the object moves smoothly, so we assume that R_t is twice differentiable in time, and therefore the angular velocity $\boldsymbol{\omega}_t$ is differentiable. We add to (3.3) a regularization term penalizing the variation of $\boldsymbol{\omega}_t$. Considering ρ, ϕ and ζ as functions in t, we minimize the functional

$$\tilde{\mathcal{J}}_\lambda(\rho, \phi, \zeta) = \int_0^T \left(\mathcal{J}_t(\rho_t, \phi_t, \zeta_t) + \lambda \mathcal{G}_t(\rho, \phi, \zeta)\right) \mathrm{d}t \tag{3.5}$$

with some regularization parameter $\lambda > 0$ and

$$\mathcal{G}_t(\rho, \phi, \zeta) \coloneqq \|\partial_t \boldsymbol{\omega}(\rho_t, \phi_t, \zeta_t)\|^2 = \left\| \partial_t \begin{pmatrix} \rho_t \cos \phi_t \\ \rho_t \sin \phi_t \\ \zeta_t \end{pmatrix} \right\|^2 = (\rho_t')^2 + |\rho_t|(\phi_t')^2 + (\zeta_t')^2.$$

A straightforward calculation shows the following formulas for the derivatives of $\tilde{\mathcal{J}}_\lambda$.

Lemma 3.2. *Let $\lambda > 0$, $\phi \in C^2([0,T] \to [0,\pi))$, and $\rho, \zeta \in C^2([0,T] \to \mathbb{R})$. The functional derivatives of $\tilde{\mathcal{J}}_\lambda$ are given by*

$$\begin{aligned}
\delta_\rho \tilde{\mathcal{J}}_\lambda(\rho, \phi, \zeta) &= \int_0^T \left(\partial_\rho \mathcal{J}_t(\rho_t, \phi_t, \zeta_t) - 2\lambda \rho_t'' + \lambda (\phi_t')^2 \right) \mathrm{d}t, \\
\delta_\phi \tilde{\mathcal{J}}_\lambda(\rho, \phi, \zeta) &= \int_0^T \partial_\phi \mathcal{J}_t(\rho_t, \phi_t, \zeta_t) - 2\lambda \rho_t \phi_t'' \, \mathrm{d}t, \\
\delta_\zeta \tilde{\mathcal{J}}_\lambda(\rho, \phi, \zeta) &= \int_0^T \partial_\zeta \mathcal{J}_t(\rho_t, \phi_t, \zeta_t) - 2\lambda \zeta_t'' \, \mathrm{d}t,
\end{aligned}$$

where

$$\begin{aligned}
\partial_\rho \mathcal{J}_t(\rho, \phi, \zeta) &= -2 \int_{-k_0}^{k_0} p_\phi(r) \left(g_\phi(r) - \rho p_\phi(r) - \zeta q_\phi(r) \right) \mathrm{d}r, \\
\partial_\phi \mathcal{J}_t(\rho, \phi, \zeta) &= 2 \int_{-k_0}^{k_0} (g_\phi(r) - \rho p_\phi(r) - \zeta q_\phi) \Big(r \partial_\phi \partial_t - \Big(\frac{\rho}{r} (k_0^2 - \sqrt{k_0^2 - r^2}) + \zeta \Big) \partial_\phi^2 \Big) \nu_t(r\boldsymbol{\phi}) \, \mathrm{d}r, \\
\partial_\zeta \mathcal{J}_t(\rho, \phi, \zeta) &= -2 \int_{-k_0}^{k_0} q_\phi(r) \left(g_\phi(r) - \rho p_\phi(r) - \zeta q_\phi(r) \right) \mathrm{d}r.
\end{aligned}$$

We minimize (3.5) using gradient descent with step-width $\alpha > 0$. We assume to have a starting solution $\rho^{(0)} \in \mathbb{R}$, $\phi^{(0)} \in [0, \pi)$, and $\zeta^{(0)} \in \mathbb{R}$, e.g. from Algorithm 1, and set

$$\begin{aligned}
\rho^{(k+1)} &= \rho^{(k)} - \alpha \partial_\rho \mathcal{J}_t(\rho^{(k)}, \phi^{(k)}, \zeta^{(k)}), \\
\phi^{(k+1)} &= \phi^{(k)} - \alpha \partial_\phi \mathcal{J}_t(\rho^{(k)}, \phi^{(k)}, \zeta^{(k)}), \\
\zeta^{(k+1)} &= \phi^{(k)} - \alpha \partial_\zeta \mathcal{J}_t(\rho^{(k)}, \phi^{(k)}, \zeta^{(k)}).
\end{aligned} \tag{3.6}$$

3.1.3 Rotation Matrix

Following [34], we compute the rotation R_t with given angular velocity $\boldsymbol{\omega}_t$ by solving the initial value problem (2.15) with the forward *Euler method* on $\mathbb{R}^{3\times 3}$ followed by a projection to SO(3) in each step. More precisely, denote the singular value decomposition (SVD) of a matrix $A \in \mathbb{R}^{3\times 3}$ by $A = U\Sigma V^\top$, and set $\mathrm{Polar}(A) \coloneqq UV^\top$. The orthogonal projection P_Q of the tangent space

$$\mathcal{T}_Q \mathrm{SO}(3) \coloneqq \{QS : S \in \mathbb{R}^{3\times 3},\ S = -S^\top\}$$

of SO(3) at $Q \in \mathrm{SO}(3)$ onto SO(3) with respect to the Frobenius norm is given by

$$\mathrm{P}_Q(W) \coloneqq \mathrm{Polar}(Q + W) \in \mathrm{SO}(3), \qquad Q \in \mathrm{SO}(3),\ W \in \mathcal{T}_Q \mathrm{SO}(3),$$

cf. [26]. Using integer time steps $t = 0, 1, \ldots, T$ and assuming that $R_0 \in \mathrm{SO}(3)$ is given, we approximate the rotation R_t by

$$\begin{aligned}
\mathbf{R}_0 &\coloneqq R_0, \\
\mathbf{R}_{t+1} &\coloneqq \mathrm{P}_{\mathbf{R}_t}(\mathbf{R}_t W_t).
\end{aligned} \tag{3.7}$$

3.2 Regularized Direct Common Circle Method

The direct method solves (2.9) and (2.10) to find the Euler angles $\varphi \in [0, 2\pi)$, $\theta \in [0, \pi]$, $\psi \in [0, 2\pi)$ of the incremental rotation $R_s^\top R_t$. We minimize the least-squares functional

$$\mathcal{E}_{s,t}(\varphi, \theta, \psi) := \int_{-\pi/2}^{\pi/2} \left|\nu_t(\boldsymbol{\gamma}^{\pi-\psi,\theta}(-\beta)) - \nu_s(\boldsymbol{\gamma}^{\varphi,\theta}(\beta))\right|^2 + \left|\nu_t(\boldsymbol{\gamma}^{*,\pi-\psi,\theta}(\beta)) - \nu_s(\boldsymbol{\gamma}^{*,\varphi,\theta}(\beta))\right|^2 \mathrm{d}\beta \tag{3.8}$$

over $\varphi, \psi \in [0, 2\pi)$ and $\theta \in [0, \pi]$, cf. [34]. The true Euler angles (2.8) of $R_s^\top R_t$ constitute a global minimizer of $\mathcal{E}_{s,t}$. However, there is no theoretical guarantee that $\mathcal{E}_{s,t}$ has only one global minimum. For noisy measurements, $\mathcal{E}_{s,t}$ might have a global minimum not corresponding to the true rotation. Furthermore, the optimization becomes quite hard as $\mathcal{E}_{s,t}$ is non-convex and there may exist many local minima.

Contrary to [34], we assume that we already have an estimate $\tilde{R}_t$ of R_t, and therefore $R_s^\top R_t$ is in the proximity of $\tilde{R}_s \tilde{R}_t$. This estimate can come e.g. from the infinitesimal method of Section 3.1. We denote the angle of a rotation $Q \in \mathrm{SO}(3)$ by

$$\angle(Q) = \arccos((\mathrm{trace}(Q) - 1)/2) \in [0, \pi], \tag{3.9}$$

which induces a distance of two rotations on SO(3) via

$$d(R, Q) = \angle(R^\top Q), \qquad R, Q \in \mathrm{SO}(3).$$

Then, we add to (3.8) as regularization term the distance to the estimated rotation $\tilde{R}_s^\top \tilde{R}_t$, i.e.,

$$\tilde{\mathcal{E}}_{s,t}^\lambda(\varphi, \theta, \psi) := \mathcal{E}_{s,t}(\varphi, \theta, \psi) + \lambda\, d(\tilde{R}_s^\top \tilde{R}_t, Q^{(3)}(\varphi) Q^{(2)}(\theta) Q^{(3)}(\psi)), \tag{3.10}$$

with a regularization parameter $\lambda > 0$. Then $\tilde{\mathcal{E}}_{s,t}$ can be minimized via a standard algorithm like gradient descent. The integral (3.8) can be discretized via quadrature, and ν_t needs to be interpolated if it is given on a grid.

4 Numerics

For $N \in \mathbb{N}$, define the grid

$$\mathcal{I}_N := \{-\tfrac{N}{2}, \dots, \tfrac{N}{2} - 1\},$$

and denote the pixel size by $p > 0$. We have a video of the (complex-valued) total field

$$u_t^{\mathrm{tot}}(\boldsymbol{x}) = u^{\mathrm{inc}}(\boldsymbol{x}) + u_t(\boldsymbol{x}), \qquad \forall \boldsymbol{x} \in p\mathcal{I}_N^2,\ t = 0, \dots, T-1,$$

i.e. the sum of incidence field u^{inc} from (2.1) and scattered field u_t. The time index $t = 0, \dots, T-1$ corresponds to the t-th frame of the video. It is convenient to decompose

$$u_t^{\mathrm{tot}}(\boldsymbol{x}) = a_t(\boldsymbol{x})\, \mathrm{e}^{\mathrm{i}\varphi_t(\boldsymbol{x})}$$

into its amplitude $a_t(\boldsymbol{x}) = |u_t^{\mathrm{tot}}(\boldsymbol{x})|$ and phase $\varphi_t(\boldsymbol{x})$. For the latter, a phase unwrapping needs to be performed in general, cf. [5, 12], but is not necessary in our examples. We emphasize that the complex field is measured and therefore no phase retrieval is required as opposed to [2, 25].

4.1 Data Preprocessing

Renormalization and estimation of the incidence field: By (2.1), the incident field u^{inc} at the measurement plane is $\mathrm{e}^{\mathrm{i}k_0 r_{\mathrm{M}}}$. To compute the scattered field $u = u^{\mathrm{tot}} - u^{\mathrm{inc}}$, we assume the incident field u^{inc} to be constant over the whole measurement plane, but it might vary slightly over time t due to data acquisition effects. We approximate the incident field by $u_t^{\mathrm{inc}} \approx \mathrm{e}^{\mathrm{i}\varphi_t^{\mathrm{med}}}$,

where φ_t^{med} is the median of the phase $\{\varphi_t(\boldsymbol{x}) : \boldsymbol{x} \in p\mathcal{I}_N^2\}$. The median over the whole recorded image should be unaffected by the values inside the object. Theoretically, one would need to consider φ on the 2π-periodic torus, but this is not necessary here as the phase only varies moderately. We have

$$u_t(\boldsymbol{x}) = u_t^{\text{tot}}(\boldsymbol{x}) - u_t^{\text{inc}} \approx a_t(\boldsymbol{x})\, \mathrm{e}^{\mathrm{i}\varphi_t(\boldsymbol{x})} - \mathrm{e}^{\mathrm{i}\varphi_t^{\text{med}}}.$$

Rytov approximation: The Rytov approximation assumes that the phase gradient is small and therefore often yields more accurate results than the Born approximation, which assumes the total phase change to be small, cf. [15, 28]. Mathematically, it corresponds to a transformation of the measurement data, then the reconstruction can be done exactly as with the Born approximation used in the theoretical derivations, see [11]. Setting a_t^{med} as the median of the amplitude a_t, we use as our Rytov data

$$u_t^{\text{Rytov}}(\boldsymbol{x}) = u_t^{\text{inc}} \cdot \left(\mathrm{i}(\varphi_t(\boldsymbol{x}) - \varphi_t^{\text{med}}) + \log\left(\frac{a_t(\boldsymbol{x})}{a_t^{\text{med}}} \right) \right).$$

Soft cutoff: We first cut out the images to a square so that the object is approximately in the center. As the outer part of the images contains mainly noise and no object information, we apply the soft, circular cutoff C^1 function

$$c_{r_1,r_2}(\boldsymbol{x}) = \begin{cases} 1, & |\boldsymbol{x}| \le r_1, \\ \frac{(r_2 - |\boldsymbol{x}|)^2 (2|\boldsymbol{x}| + r_2 - 3r_1)}{(r_2 - r_1)^3}, & r_1 < |\boldsymbol{x}| < r_2, \\ 0, & |\boldsymbol{x}| \ge r_2, \end{cases}$$

with parameters $r_2 > r_1 > 0$. We set our preprocessed, transformed measurements

$$m_t(\boldsymbol{x}) \coloneqq c_{r_1,r_2}(\boldsymbol{x}) u_t^{\text{Rytov}}(\boldsymbol{x}).$$

Pre-smoothing: To mitigate high-frequency noise, we apply a 3D Gaussian smoothing with standard deviation 0.65 pixels to the transformed data m.

4.2 Reconstruction Steps

We estimate the rotation by the infinitesimal and the direct method. Then we can use this to reconstruct the object.

Infinitesimal common circle method: We first apply the infinitesimal method of Algorithm 1 to obtain the angular velocity $\boldsymbol{\omega}_t$. This method requires to evaluate the derivatives of $\nu_t(\boldsymbol{k}) = \frac{2}{\pi}\kappa^2(\boldsymbol{k})|\mathcal{F}_2[m_t](\boldsymbol{k})|$, see (2.7), i.e., the Fourier transform of m_t, on a polar grid $\boldsymbol{k} = (r\cos\phi, r\sin\phi)$. We approximate the Fourier transform on a polar grid using the nonuniform fast Fourier transform (NFFT) [32] of m_t, implemented in [17]. Then we compute the partial derivatives of ν_t via finite differences with the 3D analogue of the Sobel filter $\frac{1}{8}\left(\begin{smallmatrix} -1 & -2 & -1 \\ 0 & 0 & 0 \\ 1 & 2 & 1 \end{smallmatrix}\right)$.

We improve this first estimate of the angular velocity $\boldsymbol{\omega}_t$ by minimizing (3.5) using the gradient descent (3.6) with 50 iterations, $\lambda = 0.1$, and $\alpha = 10^{-10}$. From the resulting new estimate of $\boldsymbol{\omega}_t$, we obtain the rotations R_t by (3.7).

Direct common circle method: We minimize the regularized functional (3.10). As starting solution $\tilde{R}_t$, we use our reconstructed rotations from the infinitesimal method. The integral in (3.8) is approximated by 200 equidistant points β, and the function ν_t is evaluated on arbitrary points via a cubic spline interpolation. We minimize (3.10) with the Nelder–Mead downhill

simplex method implemented in Matlab's `fminsearch`. We also tested a gradient-based optimizer, which usually gave similar results and computation times.

We go three times over all time steps. The direct method encounters instabilities when the rotations R_t and R_s are too similar or differ by nearly 180 °, because the measured hemispheres are close together. Therefore, we choose $t - s$ in a range such that neither occurs. As the motion is approximately periodical, we obtain a rough estimate of the number of frames for a full rotation by maximizing the correlation between the images m_t. This way we have an estimate for which $|s - t|$ we can expect $R_t \approx R_s$. Because the direct method is instable for small rotations, we do not use it for the first few time steps t. Instead, we linearly interpolate (in the rotation angle) between the rotations. As final postprocessing, we apply a mean filter with respect to time t to the reconstructed rotations R_t.

Translations: Object translations, see (2.6), do not affect the reconstruction of the rotations, because ν_t is translation-invariant; they only affect the object reconstruction. In many subsequent examples, the translational shifts are small enough to be negligible. We estimate such shifts by the following circle fitting approach. We first preprocess $|u_t|$ with a median filter, and perform a circle fitting (in Matlab's imaging toolbox) on regions of the image where $|u_t|$ exceeds a threshold. The estimated shift is determined by the center of the fitted circle or ellipse. Finally, we interpolate the image using these estimated shifts.

Object reconstruction: Having estimated the rotations R_t in the previous step and the measurements m_t, we reconstruct the scattering potential f using the inverse NDFT (nonuniform discrete Fourier transform) method with 12 conjugate gradient iterations, as described in [1, sect 5.2] and implemented in Matlab.* Then, by (2.2), we calculate from f the refractive index

$$n(\boldsymbol{x}) = n_0 \sqrt{\frac{f(\boldsymbol{x})}{k_0^2} + 1}.$$

4.3 In Silico Phantom with Beam Propagation Method

We simulate a phantom refractive index $n(\boldsymbol{x})$ consisting of a large ellipsoid with a major axis of 6 µm and constant refractive index containing many small balls with higher refractive index, see Figure 2a. This object has similar parameters and shape as the Neuroblastoma cell we will consider in subsubsection 4.4.4 below. In order to avoid the so-called "inverse crime", we simulate the measurements u_t^{tot} with the beam propagation method (BPM) described in [16], see also [6, 40]. This is a non-linear model of wave propagation (2.3) that is more accurate than the (linear) Born and Rytov approximations on which the common circle method is based. We use $T = 200$ frames and a full rotation around the x_2 axis with constant angular velocity. The measurements of u^{tot} are simulated on $N \times N$ pixels with $N = 420$ and the refractive index n is discretized on $192 \times 192 \times 192$ pixels.

We assess the accuracy of the reconstructed rotation R_t^{rec} to the ground truth R_t as the angle $\angle(R_t^\top R_t^{\text{rec}})$, see (3.9), averaged over all time steps t.

We first perform the common circles method with exact data from the BPM. Here, the infinitesimal method already gives quite good results, the rotations R_t are reconstructed with an error of 6.8 ° averaged over time t, see Figure 3a. The direct common circles method gives only a minor improvement.

In order to simulate a realistic noise, we extract from measured real-world data (see below) a rectangular $N \times N \times T$ part of the video, where no object lies and thus the measurements should be constant in theory. Then we add this video to the simulated data u^{tot}, and apply the

*Matlab toolbox https://github.com/michaelquellmalz/FourierODT

preprocessing to obtain m_t, which is depicted in Figure 2b. The infinitesimal common circles method gives approximately the right direction of the angular velocity $\boldsymbol{\omega}_t$, but significantly underestimates its norm $\|\boldsymbol{\omega}_t\|$, which is the speed of rotation, yielding unsatisfactory results. This might be explained by the fact that the data consists of a superposition of the moving object and the noise, which has no rotational structure. Therefore, we apply the direct common circles method running twice through all frames. In particular, we minimize (3.10) with $\lambda = 60$, increase $s = 0, 10, 20, \ldots,$ and $t = s + 20, \ldots, s + 60$. This yields to a small error of 4.2 ° averaged over all time steps. The error of the rotations reconstructed with the common circle method for both exact and noisy data for each frame is shown in Figure 3. The reconstructed object is depicted in Figure 2c.

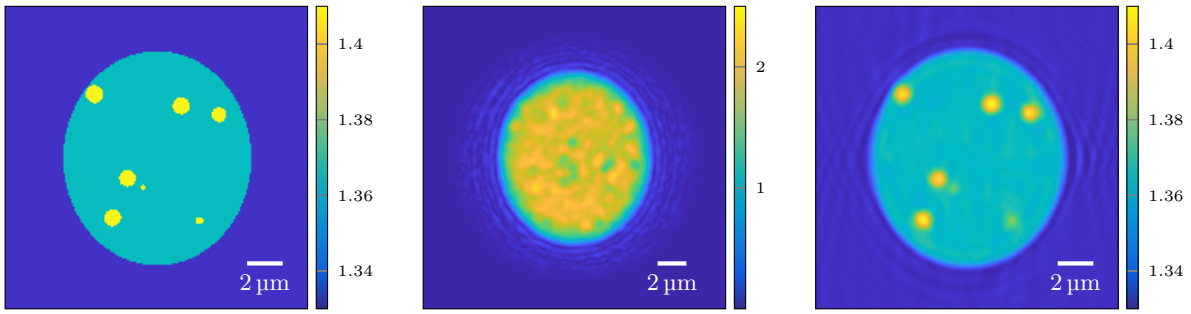

(a) Phantom $n(\boldsymbol{x})$ (b) Measurements $|m_1(\boldsymbol{x})|$ (c) Reconstruction $n(\boldsymbol{x})$

Figure 2: (a) Ground truth refractive index $n(\boldsymbol{x})$ of the phantom. (b) Absolute value of the preprocessed data $|m_t(\boldsymbol{x})|$ for $t = 1$ simulated with the BPM with added noise. (c) Reconstruction of the refractive index $n(\boldsymbol{x})$ for noisy simulated data using the Rytov approximation and the rotations reconstructed via the common circle method.

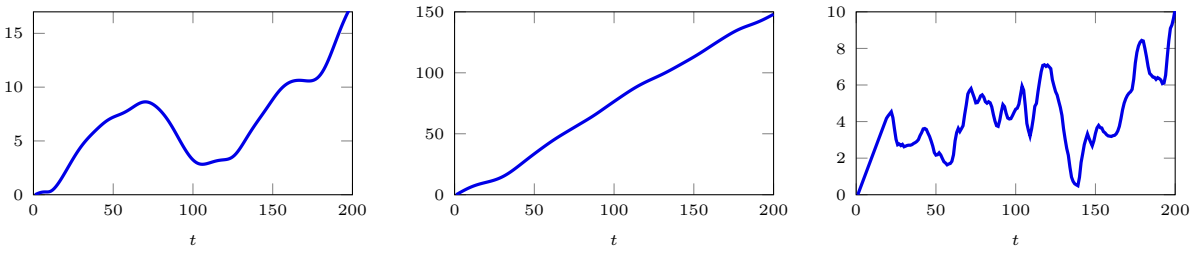

(a) Exact data, infinitesimal meth. (b) Noisy data, infinitesimal meth. (c) Noisy data, direct meth.

Figure 3: Error of the reconstructed rotation (in degree) at each frame t for the neuroblastoma phantom of Figure 2 with exact (a) or noisy data (b), (c).

4.4 Real-World Data

4.4.1 Measurement Setup

The incident wave is generated by a red laser with wavelength $\lambda_0 = 640\,\text{nm}$. The surrounding medium is water with the refractive index $n_0 = 1.33$. We assume that the image is focused at the center of the object, so we set $r_M = 0$. The measurement setup is described in detail in [27]. The object is trapped and rotated in the acoustofluidic chamber from [24], see also [21, 22]. The complex-valued data is acquired via an interferometer adapted from [13].

4.4.2 Reference Method for Comparison

The optimization approach from [27] uses a more accurate forward model similar to the beam propagation method. It optimizes simultaneously the object function f, for which it uses a TV

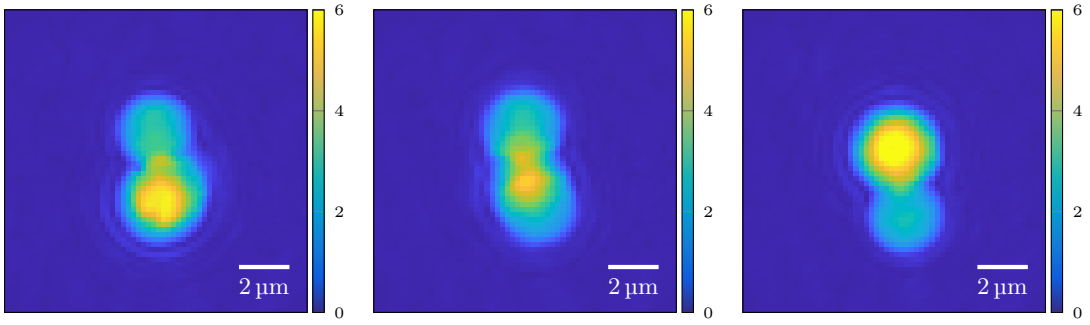

Figure 4: Absolute value of the transformed and preprocessed measurements $|m_t(\boldsymbol{x})|$ for the three-beads object dataset for time steps $t \in \{0, 5, 10\}$ (left to right).

penalty, and the motion parameters. However, it requires a somewhat decent initial solution in order to not get stuck in the wrong local minimum. We consider the reconstructions as "ground truth" for the rotations. Note that [27] uses a different coordinate system, where the light propagates in the first coordinate. Therefore, we express the rotation R in our coordinate system via the transformation

$$R = Q_0 \tilde{R}^\top Q_0^\top, \qquad Q_0 = \begin{pmatrix} 0 & 1 & 0 \\ 0 & 0 & 1 \\ 1 & 0 & 0 \end{pmatrix},$$

where $\tilde{R}$ is the rotation matrix from [27].

4.4.3 Three-Bead Object

The imaged object consists of three spherical beads, each having a constant refractive index. We have $T = 200$ frames of 60×60 pixels with a resolution of $p = 0.2\,\mu\text{m}$. The absolute value of the preprocessed data is visualized in Figure 4. A full rotation takes approximately 46 frames.

The reconstructed rotations are plotted in Figure 5. For easy visualization, we represent a rotation R as quaternion (q_0, q_1, q_2, q_3), which corresponds the rotation with angle $2 \arccos(q_0)$ around the axis $(q_1, q_2, q_3) \in \mathbb{R}^3$ and is normalized so that $\sum_{i=0}^{3} q_i^2 = 1$. The error to [27] is shown in Figure 6. The reconstructed refractive index of the object is depicted in Figure 7. We state the peak signal-to-noise ration (PSNR) and structural similarity index measure (SSIM) of the reconstructed scattering potential f to the ground truth from the optimization approach [27].

All computations are performed on an Intel Core i7-10700 with 32 GB memory. The reconstruction of the rotations took 0.4 s for the infinitesimal method and 33 s for the direct method, and the Rytov reconstruction of the object about 9 s.

4.4.4 Neuroblastoma dataset

We have a dataset of complex-valued images u_t^{tot} for a Neuroblastoma cancer cell. The measurements are on the grid $p\mathcal{I}_N$ with the pixel size $p = 0.1\,\mu\text{m}$ and $N = 250$. We use 500 frames, corresponding to slightly more than a full rotation. The absolute value of m_t in the first frame is depicted in Figure 9a.

Whereas in the previous examples, we neglected translations of the object, the Neuroblastoma sample moves slightly in the image plane, so we estimate the shifts via the circle fitting method from Section 4.2. This circle fitting method produces similar results as [27], see Figure 9b.

The reconstruction of the object f has the freedom of a rotation of the coordinate system, which may differ between the considered methods. To make a fair comparison, we adjusted the

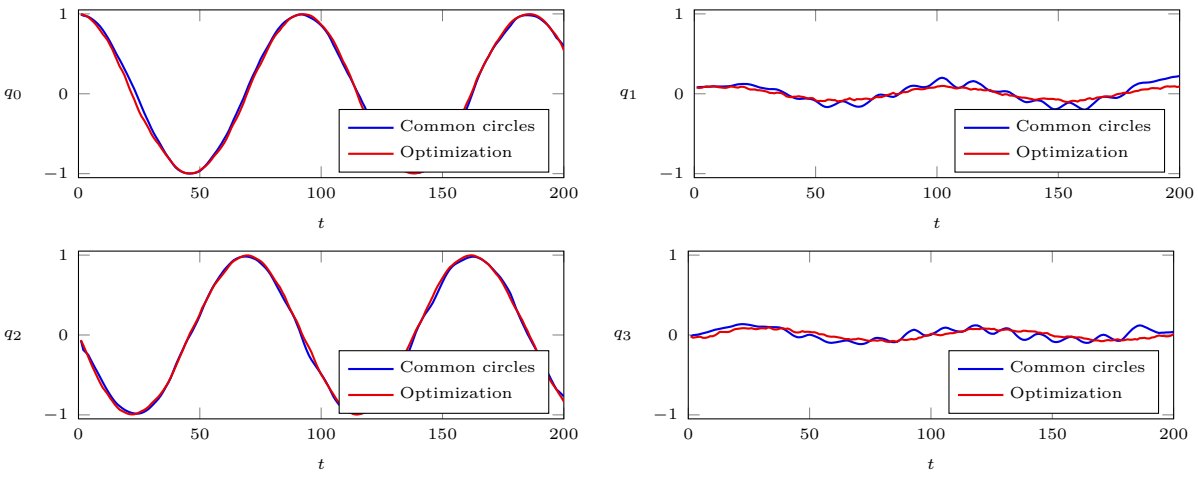

Figure 5: Reconstructed rotations for three-beads object. The four plots are the components of the quaternions. Blue: Common circle method. Red: Optimization approach [27].

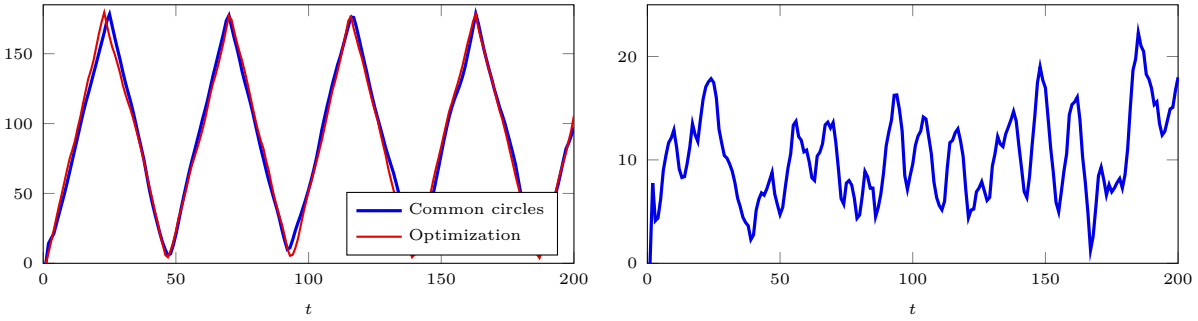

Figure 6: Three-beads object. Left: Rotation angle $\angle(R_t R_0^\top)$ in degrees. Right: Angle $d(R_t^{\mathrm{CC}}, R_t^{\mathrm{Opt}})$ in degrees between the rotation R_t^{CC} reconstructed with the common circle method and the Optimization approach R_t^{Opt} [27]. The average over all time steps is 10.3 °.

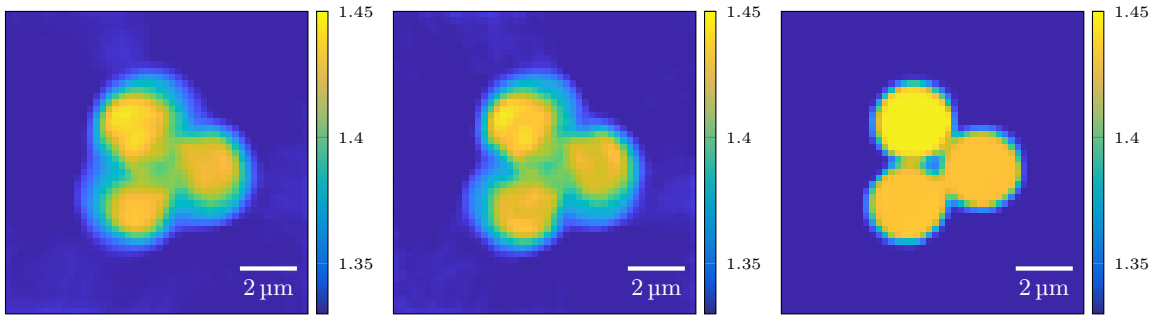

Figure 7: Reconstructed refractive index $n(\boldsymbol{x})$ for the Three-Beads object. Left: Rytov reconstruction with rotations from common circle method (PSNR 21.3, SSIM 0.669). Center: Rytov reconstruction with rotations from [27] (PSNR 21.3, SSIM 0.682). Right: Reconstruction with the optimization approach.

reconstructed object f_{Opt} from [27] by a global rotation and translation, which we estimated by minimizing the least-squares fit $\sum_{\boldsymbol{x}} |f_{\mathrm{Rytov}}(\boldsymbol{x}) - f_{\mathrm{Opt}}(R_{\mathrm{glob}}\boldsymbol{x} - \boldsymbol{c})|^2$ over $R_{\mathrm{glob}} \in \mathrm{SO}(3)$ and $\boldsymbol{c} \in \mathbb{R}^3$. Hence we replace f_{Opt} by $f_{\mathrm{Opt}}(R_{\mathrm{glob}} \cdot -\boldsymbol{c})$.

The reconstructed rotations are shown in Figure 10. In Figure 11, we see the distance between the reconstructed rotations and the ones from [27] corrected for the global mismatch. The reconstructed refractive index is shown in Figure 12. Note that the reconstruction from [27] uses

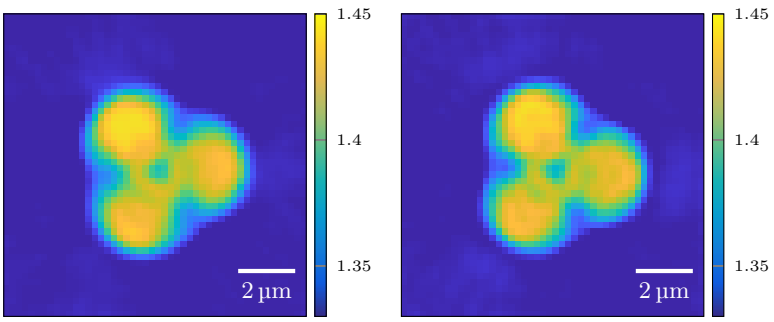

Figure 8: Reconstructed refractive index $n(\boldsymbol{x})$ for the Three-Beads object incorporating the reconstructed translations from [27]. Left: Rytov reconstruction with rotations from common circle method (PSNR 24.3, SSIM 0.704). Right: Rytov reconstruction with rotations from [27] (PSNR 27.0, SSIM 0.744).

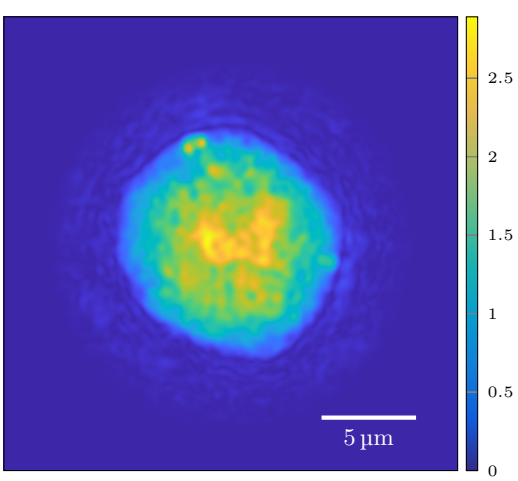

(a) Absolute value of preprocessed measurements $|m_t(\boldsymbol{x})|$ at the first frame $t = 0$.

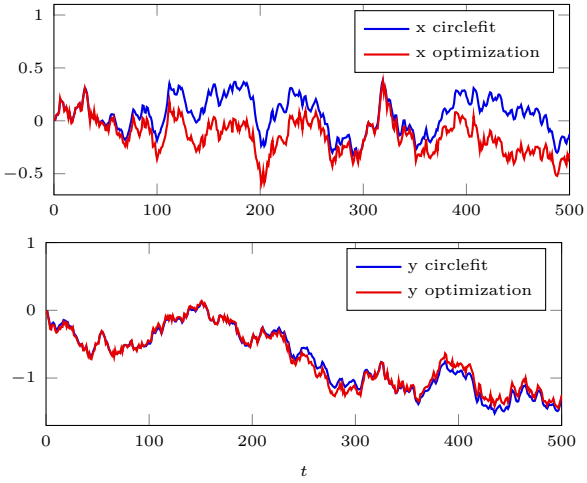

(b) Translations in x direction (top) and y direction (bottom) reconstructed via circle fitting (blue) or the optimization approach [27] (red).

Figure 9: Visualization of Neuroblastoma dataset and reconstructed translations.

a total variation prior, which makes the image look smoother.

5 Conclusions

We have demonstrated the practical application of the common circle method for motion detection in optical diffraction tomography using experimental data. By introducing temporal regularization and ensuring consistency across time steps, we achieved stable motion estimation, which allowed for the accurate 3D reconstruction of the refractive index in biological samples.

Moving forward, we aim to automate the reconstruction pipeline and develop a hybrid approach combining the speed and initialization-free nature of the common circle method with the precision of full optimization technique [27]. Such a framework would be beneficial for imaging larger objects efficiently. In order to enhance noise robustness, we want to utilize sliced optimal transport [1, 30, 33], extending methods for rigid alignment of planes [35] and synchronizing rotations [3].

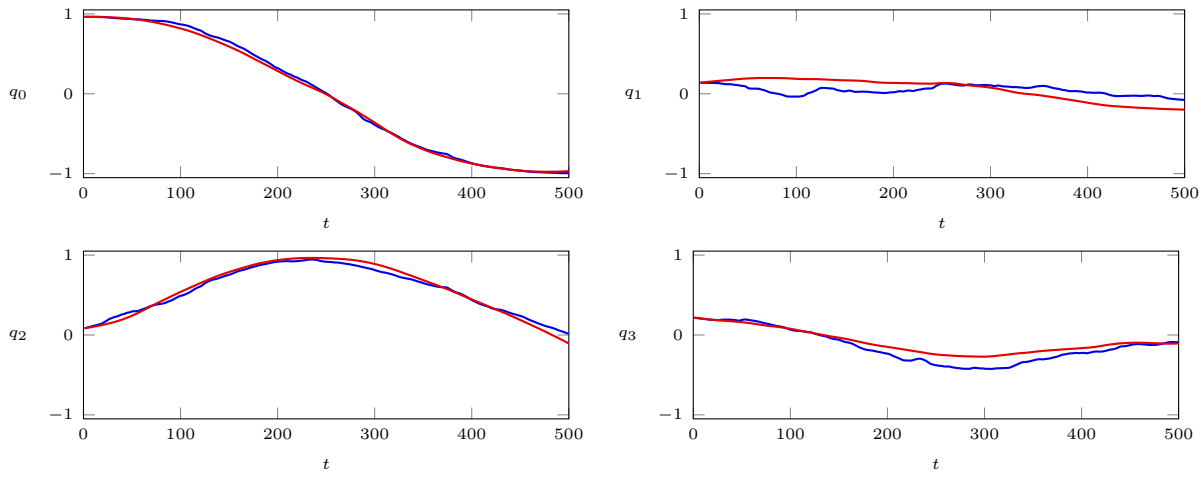

Figure 10: Reconstructed rotations for the Neuroblastoma. The four plots are the components of the quaternions. Blue: Common circle method. Red: Optimization approach [27].

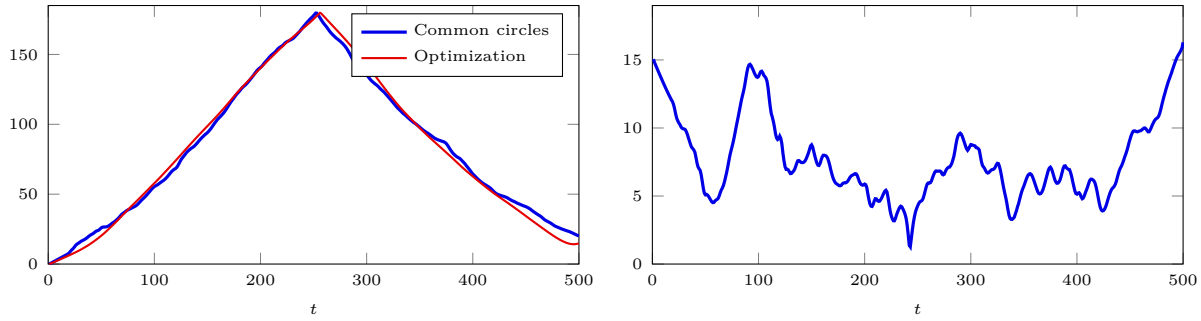

Figure 11: Reconstructed rotations for the Neuroblastoma. Left: Rotation angle $d(R_t, R_0)$ in degrees. Right: Angle $d(R_t^{\mathrm{CC}}, R_t^{\mathrm{Opt}})$ in degrees between the rotation R_t^{CC} reconstructed with the common circle method and R_t^{Opt} with the Optimization approach [27], the average over all time steps is 7.7 °.

Acknowledgments

Funding by the DFG under the SFB "Tomography Across the Scales" (STE 571/19-1, project number: 495365311) is gratefully acknowledged. Moreover, MKL and MRM are supported by the Austrian Science Fund (FWF), with SFB 10.55776/F68 "Tomography Across the Scales", project F6806-N36 Inverse Problems in Imaging of Trapped Particles (MRM). For the purpose of open access, the authors have applied a CC BY public copyright license to any authors-accepted manuscript version arising from this submission.

We thank Judith Hagenbuchner and Michael Ausserlechner (both Dept. of Pediatrics I and 3D Bioprinting Lab, Medical University Innsbruck) for providing us with the neuroblastoma sample. Furthermore, we thank Peter Elbau, Otmar Scherzer, Denise Schmutz (all University of Vienna) and Gabriele Steidl (TU Berlin) for fruitful conversations about the common circles method.

Data Availability Statement The data that support the findings of this study are available from the corresponding author upon reasonable request.

References

[1] R. Beinert and M. Quellmalz. Total variation-based reconstruction and phase retrieval for diffraction tomography. *SIAM Journal on Imaging Sciences*, 15(3):1373–1399, 2022. doi:10.1137/22M1474382.

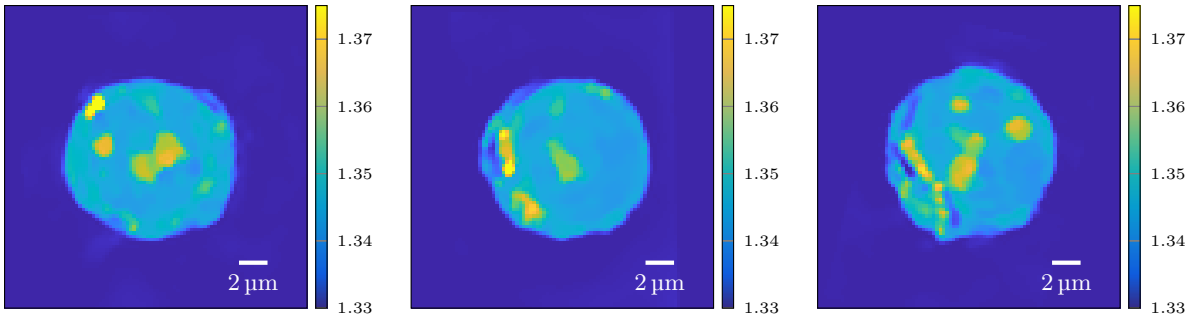

(a) Reconstruction by optimization approach [27] (taken as ground truth).

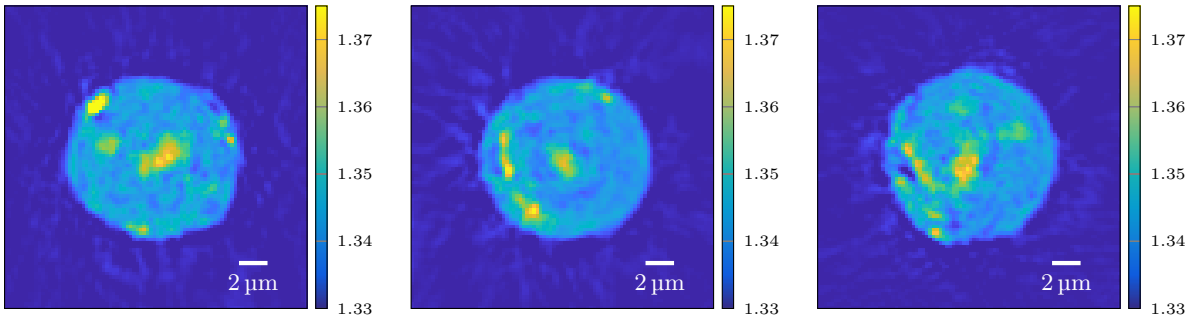

(b) Rytov reconstruction with rotations from common circle method and translations from the circle fitting (PSNR 37.8, SSIM 0.900).

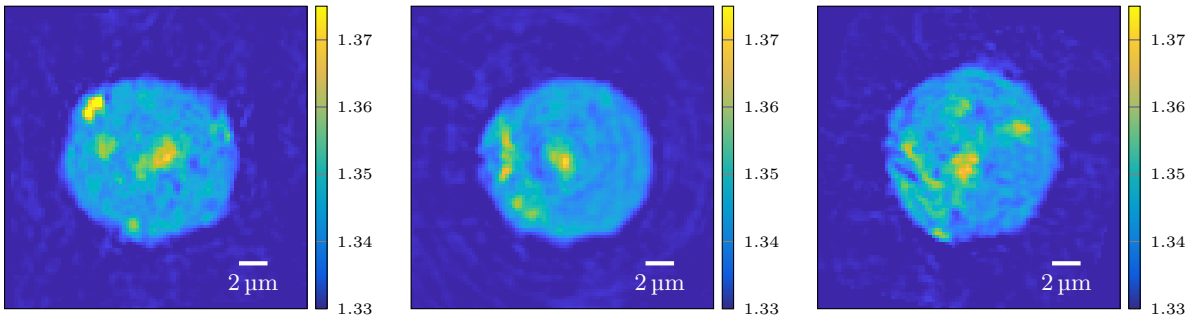

(c) Rytov reconstruction with rotations and translations from [27] (PSNR 38.5, SSIM 0.902).

Figure 12: Reconstructed refractive index $n(\boldsymbol{x})$ for the Neuroblastoma with different methods. Columns are sections through the coordinate planes (left to right: xy-plane, xz-plane, yz-plane).

[2] R. Beinert and M. Quellmalz. Total variation-based reconstruction and phase retrieval for diffraction tomography with an arbitrarily moving object. *Proceedings in Applied Mathematics & Mechanics*, 22(1), 2023. doi:10.1002/pamm.202200135.

[3] T. Birdal, M. Arbel, U. Şimşekli, and L. J. Guibas. Synchronizing probability measures on rotations via optimal transport. In *Proceedings of the IEEE/CVF Conference on Computer Vision and Pattern Recognition (CVPR)*, pages 1566–1576, 2020. doi:10.1109/CVPR42600.2020.00164.

[4] G. Bortel and M. Tegze. Common arc method for diffraction pattern orientation. *Acta Cryst.*, A67:533–543, 2011. doi:10.1107/S0108767311036269.

[5] B. Chen and J. J. Stamnes. Validity of diffraction tomography based on the first Born and the first Rytov approximations. *Applied Optics*, 37(14):2996–3006, 1998. doi:10.1364/AO.37.002996.

[6] W. Choi, C. Fang-Yen, S. Oh, N. Lue, K. Badizadegan, R. R. Dasari, and M. S. Feld. Tomographic phase microscopy—quantitative 3d imaging of living cells. *BIOforum Europe*, 11(10):24–25, 2007. doi:10.1038/nmeth1078.

[7] A. Devaney. A filtered backpropagation algorithm for diffraction tomography. *Ultrasonic Imaging*, 4(4):336–350, 1982. doi:10.1016/0161-7346(82)90017-7.

[8] K. Dholakia, B. W. Drinkwater, and M. Ritsch-Marte. Comparing acoustic and optical forces for biomedical research. *Nature Reviews Physics*, 2(9):480–491, 2020.

[9] P. Elbau, M. Ritsch-Marte, O. Scherzer, and D. Schmutz. Motion reconstruction for optical tomography of trapped objects. *Inverse Problems*, 36(4):044004, 2020. doi:10.1088/1361-6420/ab67db.

[10] P. Elbau and D. Schmutz. Uniqueness of angular velocity reconstruction in parallel-beam and diffraction tomography, 2025. ArXiv 2510.18829. arXiv:2510.18829.

[11] F. Faucher, C. Kirisits, M. Quellmalz, O. Scherzer, and E. Setterqvist. Diffraction tomography, Fourier reconstruction, and full waveform inversion. In K. Chen, C.-B. Schönlieb, X.-C. Tai, and L. Younces, editors, *Handbook of Mathematical Models and Algorithms in Computer Vision and Imaging*, pages 273–312, Cham, 2023. Springer. doi:978-3-030-98661-2_115.

[12] D. C. Ghiglia and M. D. Pritt. *Two-Dimensional Phase Unwrapping: Theory, Algorithms, and Software*. Wiley, 1998.

[13] P. Girshovitz and N. T. Shaked. Compact and portable low-coherence interferometer with off-axis geometry for quantitative phase microscopy and nanoscopy. *Opt. Express*, 21(5):5701–5714, 2013. doi:10.1364/OE.21.005701.

[14] P. H. Jones, O. M. Maragò, and G. Volpe. *Optical Tweezers*. Cambridge University Press, Cambridge, 2015. doi:10.1017/CBO9781107279711.

[15] A. C. Kak and M. Slaney. *Principles of Computerized Tomographic Imaging*. Number 33 in Classics in Applied Mathematics. Society for Industrial and Applied Mathematics (SIAM), Philadelphia, PA, 2001. Reprint of the 1988 original.

[16] U. S. Kamilov, I. N. Papadopoulos, M. H. Shoreh, A. Goy, C. Vonesch, M. Unser, and D. Psaltis. Optical tomographic image reconstruction based on beam propagation and sparse regularization. *IEEE Trans. Comput. Imaging*, 2(1):59–70, 2016. doi:10.1109/TCI.2016.2519261.

[17] J. Keiner, S. Kunis, and D. Potts. NFFT 3.5, C subroutine library. https://www.tu-chemnitz.de/~potts/nfft. Contributors: F. Bartel, M. Fenn, T. Görner, M. Kircheis, T. Knopp, M. Quellmalz, M. Schmischke, T. Volkmer, A. Vollrath.

[18] C. Kirisits, M. Quellmalz, M. Ritsch-Marte, O. Scherzer, E. Setterqvist, and G. Steidl. Fourier reconstruction for diffraction tomography of an object rotated into arbitrary orientations. *Inverse Problems*, 37(11):115002, 2021.

[19] C. Kirisits, M. Quellmalz, and E. Setterqvist. Generalized Fourier diffraction theorem and filtered backpropagation for tomographic reconstruction. *SIAM Journal on Imaging Sciences*, 2025. doi:10.1137/24M167370X.

[20] P. Kurlberg and G. Zickert. Formal uniqueness in Ewald sphere corrected single particle analysis. *ArXiv 2104.05371*, 2021.

[21] M. Kvåle Løvmo, B. Pressl, G. Thalhammer, and M. Ritsch-Marte. Controlled orientation and sustained rotation of biological samples in a sono-optical microfluidic device. *Lab on a Chip*, 21(8):1563–1578, 2021. doi:10.1039/D0LC01261K.

[22] M. Kvåle Løvmo, B. Pressl, G. Thalhammer, and M. Ritsch-Marte. A 'sono-optical' microfluidic device for induced sustained rotation and manipulation of biological samples. In P. Ferraro, S. Grilli, M. Ritsch-Marte, and C. K. Hitzenberger, editors, *Optical Methods for Inspection, Characterization, and Imaging of Biomaterials V*. SPIE, 2021. doi:10.1117/12.2595717.

[23] M. Kvåle Løvmo, S. Deng, S. Moser, R. Leitgeb, W. Drexler, and M. Ritsch-Marte. Ultrasound-induced reorientation for multi-angle optical coherence tomography. *Nature Communications*, 15:2391, 2024. doi:10.1038/s41467-024-46506-2.

[24] M. K. Løvmo, S. Moser, G. Thalhammer-Thurner, and M. Ritsch-Marte. Acoustofluidic trapping device for high-NA multi-angle imaging. *Frontiers in Physics*, 10, 2022. doi:10.3389/fphy.2022.940115.

[25] M. H. Maleki and A. J. Devaney. Phase-retrieval and intensity-only reconstruction algorithms for optical diffraction tomography. *Journal of the Optical Society of America A*, 10(5):1086–1092, 1993.

[26] M. Moakher. Means and averaging in the group of rotations. *SIAM Journal on Matrix Analysis and Applications*, 24(1):1–16, 2002. doi:10.1137/s0895479801383877.

[27] S. Moser, M. K. Løvmo, F. Strasser, J. Hagenbuchner, M. J. Ausserlechner, and M. Ritsch-Marte. Optical tomography reconstructing 3d motion and structure of multiple-scattering samples under rotational actuation. *Optica*, 12(5):594–603, 2025. doi:10.1364/OPTICA.550450.

[28] P. Müller, M. Schürmann, and J. Guck. The theory of diffraction tomography, 2015. ArXiv 1507.00466v3. arXiv:1507.00466.

[29] F. Natterer and F. Wübbeling. *Mathematical Methods in Image Reconstruction*. Number 5 in Monographs on Mathematical Modeling and Computation. SIAM, Philadelphia, PA, 2001.

[30] K. Nguyen. An introduction to sliced optimal transport: Foundations, advances, extensions, and applications. *Foundations and Trends in Computer Graphics and Vision*, 17(3-4):171–406, 2025.

[31] P. A. Penczek, J. Zhu, and J. Frank. A common-lines based method for determining orientations for $n > 3$ particle projections simultaneously. *Ultramicroscopy*, 63(3-4):205–218, 1996. doi:10.1016/0304-3991(96)00037-x.

[32] G. Plonka, D. Potts, G. Steidl, and M. Tasche. *Numerical Fourier Analysis*. Applied and Numerical Harmonic Analysis. Birkhäuser, Cham, 2018. doi:10.1007/978-3-030-04306-3.

[33] M. Quellmalz, L. Buecher, and G. Steidl. Parallelly sliced optimal transport on spheres and on the rotation group. *Journal of Mathematical Imaging and Vision*, 66:951–976, 2024. doi:10.1007/s10851-024-01206-w.

[34] M. Quellmalz, P. Elbau, O. Scherzer, and G. Steidl. Motion detection in diffraction tomography by common circle methods. *Mathematics of Computation*, 93:747–784, 2024. doi:10.1090/mcom/3869.

[35] Y. Shi, A. Singer, and E. J. Verbeke. Fast rigid alignment of heterogeneous images in sliced Wasserstein distance, 2025. ArXiv 2503.13756. arXiv:2503.13756.

[36] A. Singer, R. R. Coifman, F. J. Sigworth, D. W. Chester, and Y. Shkolnisky. Detecting consistent common lines in cryo-EM by voting. *Journal of Structural Biology*, 169(3):312–322, 2010. doi:10.1016/j.jsb.2009.11.003.

[37] Y. Sung, W. Choi, C. Fang-Yen, K. Badizadegan, R. R. Dasari, and M. S. Feld. Optical diffraction tomography for high resolution live cell imaging. *Optics Express*, 17(1):266–277, 2009.

[38] G. Thalhammer, R. Steiger, M. Meinschad, M. Hill, S. Bernet, and M. Ritsch-Marte. Combined acoustic and optical trapping. *Biomedical Optics Express*, 2(10):2859–2870, 2011. doi:10.1364/BOE.2.002859.

[39] M. van Heel. Angular reconstitution: A posteriori assignment of projection directions for 3d reconstruction. *Ultramicroscopy*, 21(2):111–123, 1987. doi:10.1016/0304-3991(87)90078-7.

[40] J. Van Roey, J. van der Donk, and P. E. Lagasse. Beam-propagation method: analysis and assessment. *J. Opt. Soc. Am.*, 71(7):803–810, 1981. doi:10.1364/JOSA.71.000803.

[41] L. Wang, A. Singer, and Z. Wen. Orientation determination of cryo-EM images using least unsquared deviations. *SIAM Journal on Imaging Sciences*, 6(4):2450–2483, 2013. doi:10.1137/130916436.

[42] E. Wolf. Three-dimensional structure determination of semi-transparent objects from holographic data. *Optics Communications*, 1:153–156, 1969.

[43] C. Yang, Y. Yang, Y. Lin, B. Wang, Z. Qian, and S. Hirose. 2d Born approximation based linearized quantitative reconstruction method due to interlayer cavity flaws in a laminated orthotropic composite plate. In *SSRN*, 2023. doi:10.2139/ssrn.4546647.